Directional Multi-Frequency Guided Waves Communications Using Discrete Frequency-Steerable Acoustic Transducers

Directional Multi-Frequency Guided Waves Communications Using Discrete Frequency-Steerable Acoustic Transducers

Masoud Mohammadgholiha, *Member, IEEE*, Federica Zonzini, *Member, IEEE*, Jochen Moll, *Senior Member, IEEE*, and Luca De Marchi, *Senior Member, IEEE*

***Abstract*— novel directional transducer based on Guided Waves (GWs) is introduced in this paper, designed for use in structural health monitoring (SHM) and acoustic data communication applications, i.e., systems in which the elastic medium serves as a transmission channel and information is conveyed through the medium via elastic waves. novel directional transducer based on Guided Waves (GWs) is introduced in this paper, designed for use in structural health monitoring (SHM) and acoustic data communication applications, i.e., systems in which the elastic medium serves as a transmission channel and information is conveyed through the medium via elastic waves.A Such systems can overcome difficulties associated with traditional communication methods like wire-based or radio frequency (RF), which can be complex and have limitations in harsh environments or hard-to-reach places. However, the development of these techniques is hampered by GWs dispersive and multi-modal propagation and by multi-path interference. The shortcomings can be effectively addressed by employing Frequency Steerable Acoustic Transducers (FSATs), which leverage their inherent directional capabilities. This can be achieved through the exploitation of a frequency-dependent spatial filtering effect, yielding to a direct correlation between the frequency content of the transmitted or received signals and the direction of propagation. The proposed transducer is designed to actuate or sense the A0 Lamb wave propagating in three orientations using varying frequencies, and has three channels with distinct frequencies for each direction, ranging from 50 kHz to 450 kHz. The transducer performance was verified through Finite Element (FE) simulations, accompanied by experimental testing using a Scanning Laser Doppler Vibrometer (SLDV). The unique frequency-steering capability of FSATs is combined with the On-Off Keying (OOK) modulation scheme to achieve frequency directivity in hardware, similar to ongoing research in 5G communications. The MIMO capabilities of the transducer were finally tested over a thin aluminum plate, showing excellent agreement with the FE simulation results.**

***Index Terms*— Directional communication, Frequency Steerable Acoustic Transducers, Lamb waves, Structural health monitoring, Multiple-In Multiple-Out**

Masoud Mohammadgholiha, Federica Zonzini and Luca De Marchi are with the Department of Electrical, Electronic and Information Engineering, University of Bologna, 40136 Bologna, Italy (e-mail: m.mohammadgholiha@unibo.it; federica.zonzini@unibo.it; l.demarchi@unibo.it).

Jochen Moll is with Physics, Terahertz/Photonics, Goethe University of Frankfurt am Main, 60323 Frankfurt, Germany (e-mail: moll@physik.uni-frankfurt.de).

I. Introduction

Ultrasonic Guided Waves (GW) have received considerable interest in recent decades for Non-Destructive Evaluation (NDE) and Structural Health Monitoring (SHM) of pipelines, railways, aerospace structures, and other thin-walled components [1]–[3]. The extensive application of GW, and specifically Lamb waves, is due to their ability for long-range propagation with minimal energy loss as well as their multimodal behavior that enables defect detection [4], [5]. GW-based inspection systems typically consist of several piezoelectric transducers arranged and permanently attached to the structure being inspected [6]. Inspection strategies such as back propagation and inversion algorithm [7] can then be implemented through transmission and sensing of GW. Such a procedure may generate a vast amount of measured data that are subsequently processed to compute damage indicators for structural health status estimation [8], [9]. The Time Reversal Technique (TRT) [10] , for instance, back propagate the acquired data to identify and locate defects. Noticeable alternatives are the Full Matrix Capture (FMC) combined with the Total Focusing Method (TFM) [11] or the Synthetic Aperture Focusing Technique (SAFT) [12] which can be used to reconstruct damage images in complex structures.

Once computed, inspection results must be forwarded to a central data processing unit for further analysis. To this end, cable-based (or wired) transmission and radio frequency (RF) wireless communication are commonly used tools [13]. However, the former solution imposes more weight on an SHM system and, hence, more integration costs [14]. The latter, on the other hand, has limitations either in harsh environments with poor RF coverage or in hard-to-reach places, e.g., buried pipes [15]. Apart from the difficulties related to the communication channel, the potential network congestion which affects large scale installations additionally complicate the effectiveness of the information sharing process. Therefore, establishing reliable and cost-effective data transmissions and communications is of utmost importance. GW-based communications are gaining interest as an alternative solution to overcome the current limitations [16]: in these cases, the elastic medium serves as a communication channel, whereas elastic waves act as the information carrier [17].

There have been various techniques employed to address

the problem of GW data communications. One of the easiest and most effective techniques to implement wireless acoustic data transfer is offered by the On-Off Keying (OOK) modulation scheme, as demonstrated in [18]. Here, the adopted OOK approach has been further combined with Frequency-division Multiplexing (FDM) to demonstrate the feasibility of GW communication across composite plates [19]. More sophisticated solutions have also been investigated, inspired by the conventional RF-based contexts and adapted to the nature of the considered mechanical waves [17], [20]. All these methods have in common the fact that they aim at implementing Multiple-In Multiple-Out (MIMO) functionalities, the latter being desirable features in the realization of the next generation of communication systems due to the necessity to increase the channel capacity by allowing a full-duplex transmission between multiple users active at the same time [21].

Despite the efforts made so far, the development of a robust data communication system is still hampered due to GW dispersive and multi-modal propagation, as well as multi-path fading [22]. A solution to such drawbacks can be achieved by using Frequency Steerable Acoustic Transducers (FSATs), which offer inherent beam steering capabilities and selective mode excitation feature [23]. The principle of FSATs is based on a frequency-dependent spatial filtering effect which determines the direction of propagation as a function of the frequency spectrum of the signal being actuated or sensed [24]. Consequently, the FSATs effectively mitigate the effect of multi-path interference (when generated by specific boundary conditions), as opposed to conventional transducers that may experience multiple arrivals of the same transmitted waveform [25], [26]. In addition, the effects of ringing and dispersion can be minimized thanks to the spatial multiplexing capability of FSATs. In previous research [23], the transducer was designed in a way that the radiation angle continuously varied with the frequency of the propagating wave, known as Continuous FSATs. In contrast, this paper introduces a novel type of FSATs that can target specific directions with multiple frequencies, termed as Discrete FSATs , which hence possesses the unique advantage of implementing, in hardware, Multiple-In Multiple-Out functionalities without requiring several devices or external circuitry to be deployed for the same purpose.

The paper is structured as follows. Section II focuses on FSATs design by introducing the frequency-based beam steering concept, whereas Section III describes the finite element simulation of FSATs and directivity validation. In section IV, the FSATs fabrication process and the experimental results are detailed . In Section V, numerical and experimental proof of MIMO GW-driven data communication over a metallic plate is presented using FSATs and OOK, along with a systematic analysis demonstrating the robustness of the device. Lastly, the conclusion is presented in Section VI.

II. Frequency Steerable Acoustic Transducers: Working Principle and Transducer Design

A. Frequency-based Directivity Concept

The fundamental principle behind frequency-based directivity design involves analyzing the voltage measurements acquired from the electrodes of an arbitrary shape piezopatch $\Omega_p(x_1, x_2)$ under constant charge conditions [24], [27] . The voltage measurement, taking into account the stress-charge formulation of piezoelectric constitutive equations, can be represented as follows:

$$V_p = \frac{t_P}{\epsilon^{\varepsilon}_{33} A_P} \boldsymbol{b^T} e \int_{\Omega_P} \varepsilon dx_1 dx_2 \tag{1}$$

in which, ε denotes the vector representing in-plane strain components, while e stands for the piezoelectric coupling matrix under constant stress conditions. Additionally, ϵ_{33} refers to the piezo permittivity at constant strain, t_P represents the thickness of the piezo patch, and A_P denotes the area of the electrodes. The vector b enables the selection of polarization direction, which is considered here as polarized across its thickness.

The strain vector measured by the device when a plane wave propagates with angular frequency ω along a direction $\boldsymbol{i}_{1'} = \cos\theta \boldsymbol{i}_1 + \sin\theta \boldsymbol{i}_2$ can be expressed as follows [27]:

$$\varepsilon = jU_{1'_0}(\omega) e^{-jk_0(\omega)x'_1} [\ \cos^2\theta \ \ \sin^2\theta \ \ \ 0\ ]^T \equiv \varepsilon_{1'1'} \boldsymbol{r}(\theta) \tag{2}$$

substituting Eq. (2) into Eq. (1) yields:

$$V_p(\omega) = jU_{1'_0}(\omega) k_0(\omega) H(\theta) D_p(\omega, \theta) \tag{3}$$

where $U_{1'_0}(\omega)$ stands for the amplitude and polarization of the wave traveling within the plane of the structure, defined by the coordinates x_1 and x_2, at the considered angular frequency ω. k_0 represents the wave vector that defines the propagation of plane waves at an angle θ, indicating the incident wave mode's direction of arrival. The quantity H specifies the material properties of the piezo-structure system [27]:

$$H(\theta) = \frac{t_P \boldsymbol{b^T} e \boldsymbol{r(\theta)}}{A_P \epsilon^{\varepsilon}_{33}} \tag{4}$$

whereas the directivity function, denoted by D, can be written as:

$$D_p(\omega, \theta) = \int_{\Omega_P} e^{-jk_0(\omega).x} \phi_p(x) dx \tag{5}$$

in which, $\phi_p(x)$ corresponds to the load distribution function, which characterizes the shape and polarization of the transducer. In particular, D enables the selection of specific materials and polarization distributions to achieve desired directivity by tuning the transducer to specific wavelengths and corresponding wave modes. Through leveraging the bounded support of function $\phi_p(x)$, it becomes possible to extend the integration limits infinitely without impacting the integral value, which corresponds to the 2-D Fourier Transform (FT) of the function $\phi_p(x)$. Consequently, it is feasible to approximate the FT pairs, enabling the computation of directivity patterns for different transducer shapes. In essence, the suggested approach involves defining the desired directivity function in D and subsequently utilizing an inverse FT to derive the corresponding transducer geometry that takes advantage of such directional behavior [23].

In order to account for the frequency-dependent wave propagation in a waveguide, the dispersion information of the considered medium can be employed. More in detail, it has been proved that there is a possibility of having different wavenumber maxima for each propagation angle [23]. Considering Eq. (5), each maximum therefore can be associated with a specific angular frequency based on the dispersion relation $k_0(\omega)$ of the medium under consideration. It thus implies that the transducer whose frequency response is determined by the directivity function defined in Eq. (5) shall have a peak corresponding to the angular frequency associated with the incident wave direction [27]. The reciprocity of piezo sensing and actuation also enables the transducer to generate a directional wave by exciting it with a signal whose frequency content aligns with the corresponding angular frequency peak.

B. Transducer Design

As described earlier, the transducer geometry in the spatial domain follows from the wavenumber domain directivity distribution. The desired directivity distribution also depends on the transducer application. A continuous spiral directivity function was suggested in [27] and further employed in the fabrication of a Piezoceramic FSATs [23], where the radiation angle continuously varies with frequency (and hence wavenumber) of the propagating wave. In this work, by contrast, a new discrete directivity distribution is introduced, offering the opportunity to have more than one frequency in each specific direction. Such a directivity function can find application in frequency modulation-based data communication, where the carrier frequency is changed in accordance with the modulating signal.

In this study, the objective is to design an acoustic transducer that is (I) capable of actuating or sensing propagating waves along three different orientations by varying the frequency and (II) capable of having three channels, and hence distinct frequency, at each direction. As described before, the spatial distribution of material can be expressed by $\phi_p(x)$, whereas $D(k)$ represents the load distribution in the wavenumber domain. Two parameters of k and x as wavenumber and spatial vectors, respectively, can be written as:

$$\begin{aligned} k &= k_1 e_1 + k_2 e_2 \\ x &= x_1 e_1 + x_2 e_2 \end{aligned} \tag{6}$$

where two lattice vectors e_1 and e_2 define the desired wavenumbers axis. The relationship between $\phi_p(x)$ and $D(k)$ can be expressed as follows:

$$\begin{aligned} \phi_p(x_1, x_2) &= \mathcal{F}^{-1}(D(k_1, k_2)) \\ &= \iint_{\Omega_k} e^{-j(k_1 x_1 + k_2 x_2)} D(k_1, k_2) dk_1 dk_2 \end{aligned} \tag{7}$$

in which, $\mathcal{F}^{-1}$ is the 2D Inverse Fourier Transform. A schematic representing the targeted wavenumber directivity is illustrated in Fig. 1 a, showing the desired directivity maxima (blue circles) in the wavenumber domain, along with a circle with a radius of $k_{n,m}$, representing the dispersion relation at the given wavenumber. It is worth mentioning that n and m are integer values defining the targeted direction and channel

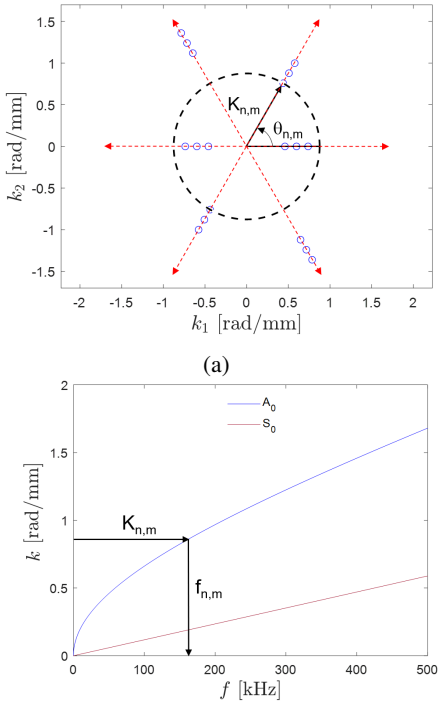

Fig. 1: Selective directionality and mode tuning: a) schematic of the proposed discrete directivity distribution in the wavenumber domain (the red dashed lines represent the desired directions); b) dispersion analysis of an Aluminum plate of 1mm thickness to obtain the corresponding frequency value of the given wavenumber

TABLE I: Desired wave directions, wavenumber, and corresponding $A0$ mode frequencies

ine Angle $\theta_{n,m}$ (°)	Wavenumber $k_{n,m}$ (rad/m)	Frequency $f_{n,m}$ (kHz)
ine 0	460	50
0	600	83
0	737	123
60	875	168
60	1015	218
60	1538	272
120	1293	329
120	1430	389
120	1570	450
ine		

index, respectively. After determining the wavenumber shape of the transducer, Eq. (7) can be utilized to recover the electrodes' spatial distribution via inverse FT.

As shown in Fig. 1 a, the maximum transducer output is computed by intersecting the medium's dispersion relation at a given wavenumber, and hence frequency, with one of the peaks in the wavenumber-domain directivity distribution, indicating the propagation direction $\theta_{n,m}$ for the considered wave vector. The dispersion relations analysis is adopted to determine the excitation frequency of the transducer $f_{n,m}$ corresponding to the given wavenumber $k_{n,m}$, as depicted in Fig. 1 b. It is important to note that the wavenumber distribution employed in the design of the proposed transducer was carefully selected

to excite only the A0 mode of the medium under consideration.

The proposed transducer is capable of generating or sensing propagating waves at three distinct angles, namely $0°$, $60°$, and $120°$. Moreover, three different wavenumber maxima are defined at each chosen direction, e.g., three channels at each direction. The selection of the wavenumber maxima was performed based on the number of channels per direction as well as the frequency bandwidth of the transducer, which is considered as $f_{min} = 50\,\text{kHz}$ and $f_{max} = 450\,\text{khz}$. As described earlier, the intersection of the wavenumber maxima with the dispersion circles indicates the wave propagation direction. The corresponding frequency values can then be obtained by employing the A0 mode dispersion relations of the considered $1\,\text{mm}$ thick aluminum plate, as depicted in Fig. 1b. Table I displays the desired wave directions, wavenumber, and associated A0 mode frequency values for all directions.

The methodology adopted to design the proposed transducer is illustrated in Fig. 2 . As depicted in Fig. 2 a, the transducer design initiates with defining the load distribution in the wavenumber domain. Subsequently, the spatial distribution is obtained through the inverse FT of the wavenumber load distribution, illustrated in Fig. 2 b. Nonetheless, practically achieving such a geometry is challenging since it necessitates continuously modulated amplitudes [28]. An effective method for overcoming this problem is to employ a three-level quantization of the spatial load distribution $\phi_p(x)$ using a specific threshold ϵ in the following method:

$$\bar{\phi_p}(x) = \begin{cases} 1 & \text{if } \phi_p(x) \geq \epsilon \\ 0 & \text{if } |\phi_p(x)| < \epsilon \\ -1 & \text{if } \phi_p(x) \leq \epsilon \end{cases} \tag{8}$$

The thresholding process indeed transforms $\phi_p(x)$ into a function $\bar{\phi_p}(x)$ with a constant value that is distributed over the domain under consideration. As a result, the patch can be subdivided into two regions with opposite polarities, yielding a two-channel transducer shape, as displayed in Fig. 2d. It should be noted that the final geometry is associated with a threshold value of 6% of the maximum of $\phi_p(x)$. The corresponding directivity is then calculated by numerically evaluating the associated FT, as shown in Fig. 2c. Although the quantization process introduces side lobes, the discrete distribution is mostly preserved, ensuring the transducer's directional properties. It is worth mentioning that the current design is limited by $180°$ ambiguity, resulting in the generation or reception of waves in two opposite directions. This is attributed to the presence of both negative and positive wavenumbers in the defined directivity distribution. It has been previously demonstrated by the authors in [23] that the estimation of the beampatterns can be achieved analytically. Therefore, the transducer performance is validated by means of Finite Element (FE) simulations, which will be presented in the following section.

III. Modeling of Frequency Steerable Acoustic Transducers

A. Simulation Methodology

In the present study, COMSOL Multiphysics® [29] is employed to develope a 3D Finite Element (FE) model of the proposed FSAT by incorporating the two principal features, namely structural mechanics and electrostatics, to assess the transducer directional capabilities. A frequency-domain simulation is adopted to validate the transducer concept as a fast solution. Time-domain analyses are further conducted in order to investigate the data communication capability of the proposed device.

B. Simulation Setup

The frequency domain simulation of wave propagation offers several advantages over time domain analysis, including the need for fewer computational resources and a shorter analysis time. In this context, the propagation medium consisting of an aluminum plate with a thickness of $1\,\text{mm}$ and dimensions $500\,\text{mm} \times 500\,\text{mm}$ was considered. As a next step, a $0.5\,\text{mm}$ thick piezoelectric (PZT) layer with dimensions $80\,\text{mm} \times 80\,\text{mm}$ was modeled as the FSAT substrate. The transducer geometry obtained during the design procedure in II was then modeled as a zero-thick line object over the PZT layer, as illustrated in Fig. 3. A thin bonding layer with a thickness of $30\,\mu\text{m}$ was employed between the PZT and the hosting aluminum plate. Of note that individual electrode segments with the same polarization (positive or negative) are connected together using wire connections. The material properties of the aluminum plate, PZT, and the bonding layer are presented in Table II. A through-thickness polarization is assumed for the PZT layer. In an effort to prevent backscattering of incident radiations, Perfectly Matched Layers (PMLs) were placed at each of the four plate boundaries. The transducer boundary conditions consisted of grounding the bottom face of the PZT and applying two opposite electrical potential boundary conditions (positive and negative input signals) to the designed electrodes on the top surface. In addition, zero charge boundary conditions were assigned to the rest of the PZT elements. The Free Quad elements were utilized to mesh both the aluminum plate and PML domains, where elements maximum size was set to $\frac{1}{10}$ of the minimum wavelength (λ_{min}) associated with the $A0$ mode within the plate. On the other hand, Free Triangular elements were employed for the transducer domains. The meshed surfaces were then swept over the thickness to create prismatic elements.

C. Simulation Results

A series of frequency domain analyses were performed by computing the steady-state response of the model under harmonic excitation [30] , which can be expressed as follows:

$$u = \hat{u}e^{j\omega t} \tag{9}$$

where u is the frequency response of the harmonic load $\hat{u}e^{jwt}$ at the angular frequency ω. To investigate this, the simulations were carried out at nine central frequencies of 50-83-123 kHz (for 0°), 168-218-272 kHz (for 60°), and 329-389-450 kHz (for 120°). It is worthwhile to mention that

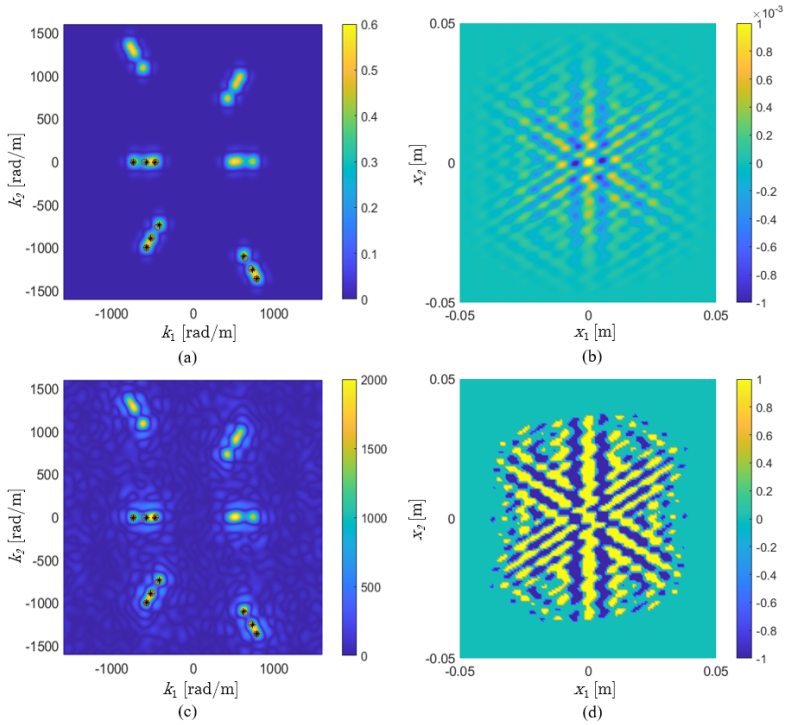

Fig. 2: FSATs design procedure: a) the load distribution in the wavenumber domain b) corresponding spatial distribution c) and d) influence of the thresholding procedure on distributions illustrated in (a) and (b), respectively

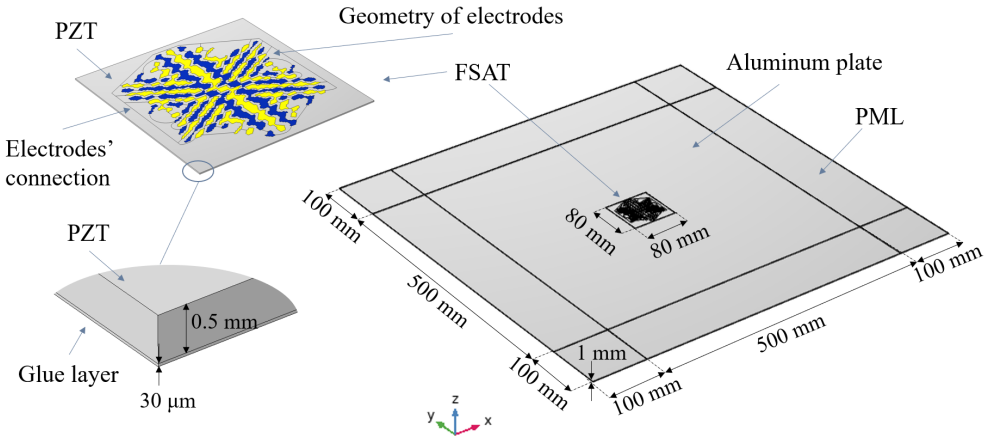

Fig. 3: 3D Finite Element (FE) model geometry

the selected frequencies only excite the $A0$ mode, according to the transducer design concept described in Section II. To demonstrate the efficiency of the simulation approach, the out-of-plane displacement magnitude of the generated Lamb waves at different frequencies is utilized. Illustrated in Fig. 4 , the acquired wavefield for the selected frequencies provides compelling evidence of the transducer's directional capabilities and its frequency dependency. More in detail, the directional wave generation is achieved by the proposed single transducer, where the amplitude of the generated wavefield at the desired directions is significantly higher compared to other directions. In addition, it can be seen that the desired wave direction depends on the actuation frequency, highlighting the frequency-based beam steering capability of the proposed transducer. Moreover, the transducer offers three distinct frequency channels for each direction, allowing for enhanced versatility and flexibility in wave generation. Note that the desired wave direction at each frequency is visually indicated by two arrows in Fig. 4.

IV. Experimental Characterization of the Proposed Transducer

A. Fabrication

In order to fabricate the proposed device, a quadratic PZT plate of $80\,\mathrm{mm}$ side length and $0.5\,\mathrm{mm}$ thickness was utilized. The PIC 255 material from PI Ceramic (Lederhose, Germany) is chosen as the core material for the PZT plate.

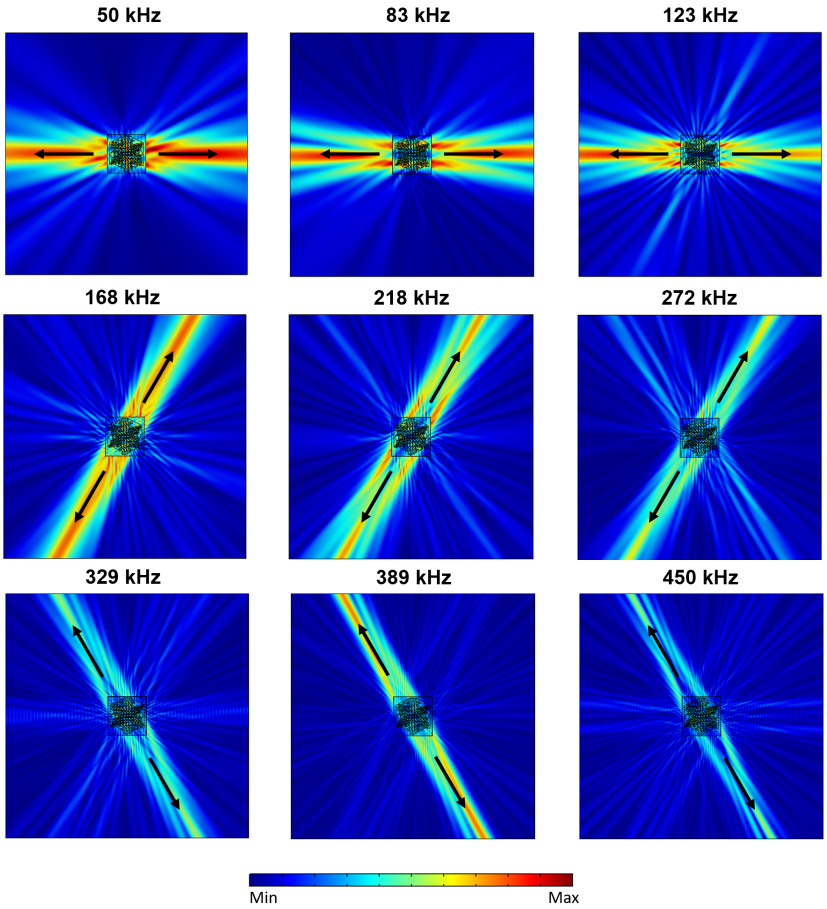

Fig. 4: Displacement magnitude of the generated waves at different directions resulting from excitation at different frequencies of 50-83-123 kHz (for 0°), 168-218-272 kHz (for 60°), and 329-389-450 kHz (for 120°) ; the black arrows indicate the desired wave directions

TABLE II: Elastic and piezoelectric properties of the materials used in the simulation

Property	Aluminum	Epoxy Glue	PIC-255
Density, ρ [kg/m^3]	2750	1150	7800
Elastic modulus [GPa]	70	4.7	$C_{11} = C_{22}$=132.7 C_{12}=86.67 C_{13}=C_{23}=85.6 C_{33}=119.2 C_{44}=C_{55}=21.3 C_{66}=22.9
Poisson ratio	0.33	0.35	-
Piezoelectric constants, d_{kij} [C/N]	-	-	d_{31} =-187 $\times$ 10^{-12} d_{33} =400 $\times$ 10^{-12} d_{15} =617 $\times$ 10^{-12}
Electrical permittivity, ϵ_{jk}	-	-	ϵ_{11}=1852 ϵ_{33}=1751

Employing the screen printing technique, electrodes were then carefully applied to the PZT plate using silver paste. Notably, one side was uniformly covered, while the other side was textured. Once the electrodes were fixed, a through-thickness poling process was executed on the PZT plate. The fabricated transducer is shown in Fig. 5.

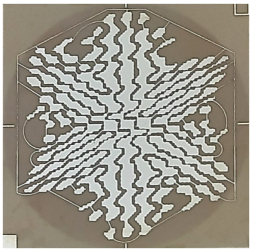

Fig. 5: The fabricated Discrete-FSAT

B. Wavefield Testing

The fabricated Discrete-FSAT was experimentally tested to assess the device directional performance. For the inspection medium, a thin square aluminum plate with a side length of 1000 mm and a thickness of 1 mm was utilized. The FSAT prototype was then attached to the aluminum plate using epoxy resin (EPO-TEK 301-2). The experimental setup, depicted in Fig 6 , consisted of a signal generator (Tektronix AFG 3022B), a power amplifier (Tegam 2350), a digital oscilloscope (Tektronix DPO 3014), and a Scanning Laser Doppler Vibrometer (SLDV) (OptoMET) equipped with a

computer. Surface wave motion can be measured precisely through SLDV, enabling non-contact and rapid guided wave measurements and visualizations [7]. Note that the SLDV was deployed perpendicular to the plate during the tests in order to acquire the plate out-of-plane displacements.

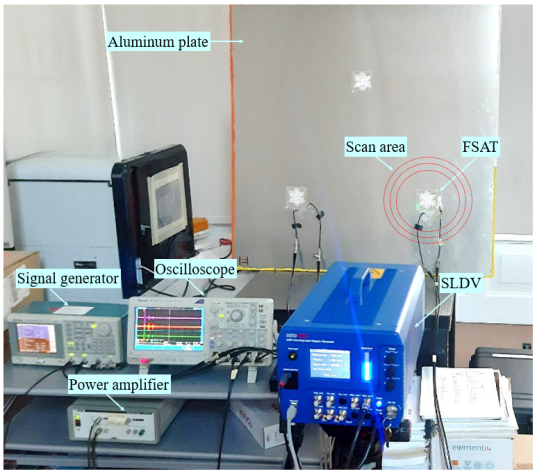

Fig. 6: The experimental test setup

The scanning area comprised three sensing circles, ranging in radii from 100 mm to 140 mm , in increments of 20 mm with sensing points each 1° centered at FSAT position. The excitation signal adopted in the form of a sine wave, featuring a peak-to-peak amplitude of 10 V at the selected frequencies listed in Table I , i.e., 50-83-123 kHz (for 0°) , 168-218-272 kHz (for 60°), and 329-389-450 kHz (for 120°) in order to calculate the beampatterns. The input signal was applied to the two electrode groups as a voltage difference relative to the common ground, as displayed in Fig. 7 . The capacitance and resistance of the two electrode groups are shown by C_1, R_1 and C_2, R_2, respectively. The capacitance C_3 represents the capacitive effect between the grounded aluminum plate and the bottom electrode of the PZT plate. It is noteworthy to mention that the bottom electrode is inaccessible. As an alternative, the aluminum plate to which the FSAT is bonded serves as a common ground.

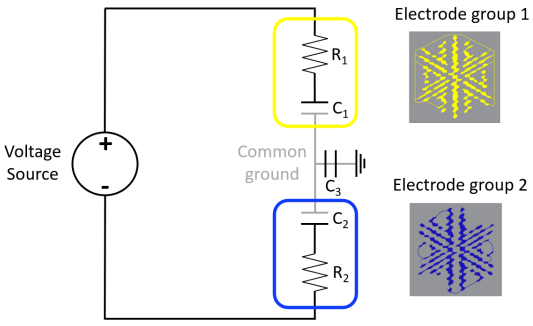

Fig. 7: Electrical diagram illustrating the differential actuation of the Discrete-FSAT

In order to show the device performance, the measured out-of-plane displacement values were used. The radiation directions, as depicted in Fig. 8 , correspond quite well with the Finite Element (FE) simulation results. The transducer radiation behavior at different frequencies is effectively validated by both the experimental findings and the FE simulation, confirming the generation of the Lamb wave $A0$ mode in 0° (for 83 kHz and 123 kHz) and in 60° (for 168 kHz). The desired wave direction at each frequency is visually represented by two arrows in Fig. 8.

The minor variation in the magnitude of the main lobes and the presence of asymmetric beam patterns can be attributed to various factors. These include reflections from the plate boundaries, variations in transducer fabrication, transducer mounting, and alignment over the aluminum plate. Additionally, the quantization process during electrode design generates a non-perfectly symmetric transducer. Collectively, these factors influence the beam pattern and account for the observed minor variations in symmetry.

V. Acoustic Data Communication

A. MIMO testing

The MIMO capabilities of the prototyped transducer were tested over a thin square aluminum plate with a thickness of 1 mm and a side length of 1000 mm. The plate was deployed with three FSATs arranged in a triangle configuration, maintaining an equal distance of 50 mm between each transducer, as displayed in Fig. 6 , which ensures communication along the 0° (Tx-RxB pair) and 60° directions (Tx-RxA), respectively. To further validate the experimental results, FE simulations of the test setup were also conducted for comparison purposes.

The OOK has been selected as a modulation technique to probe the directional capabilities of the transducer for frequency-based communication purposes. Coherently, the transmitted symbols were generated at a symbol rate of 10 ksym/s (i.e., symbol period of 100 µs) and consist in the linear superimposition of different Hann-windowed sinusoidal tones with the central frequencies of 83 kHz , 123 kHz , and 168 kHz , selecting among the ones admitted for the two considered directions. The actuation signal used in both the experiment and FE simulation is shown in Fig. 9 together with its spectrum. To perform MIMO tests, the digital oscilloscope and the commercial waveform generator introduced in Section IV-B were employed for the sake of data recording and signal actuation, correspondingly.

The decoding process was then performed on a spectrum basis by analyzing the amplitude and frequency location appearing in the spectral profile of the measured signals. Results for the transmitted 83+123+168 kHz symbol are displayed in Fig. 10, for the 0° (first column) and 60° (second column) directions. The first row depicts the experimentally received waveforms (blue curves) superimposed on the transmitted one (lilac curve)[1]: as can be observed, two clearly distinguishable wave packets magnified by red triangle markers are measured by RxB, while only one dominating peak appears along the 60°. Importantly, the distance between the location of these maxima and the relative peak of the incident wave corresponds to the expected time of flights (TOFs) for the $A0$ mode at

[1]The residual wave in the Rx signals aligned in time with the actuated symbol is due to imperfect subtraction of the electromagnetic coupling.

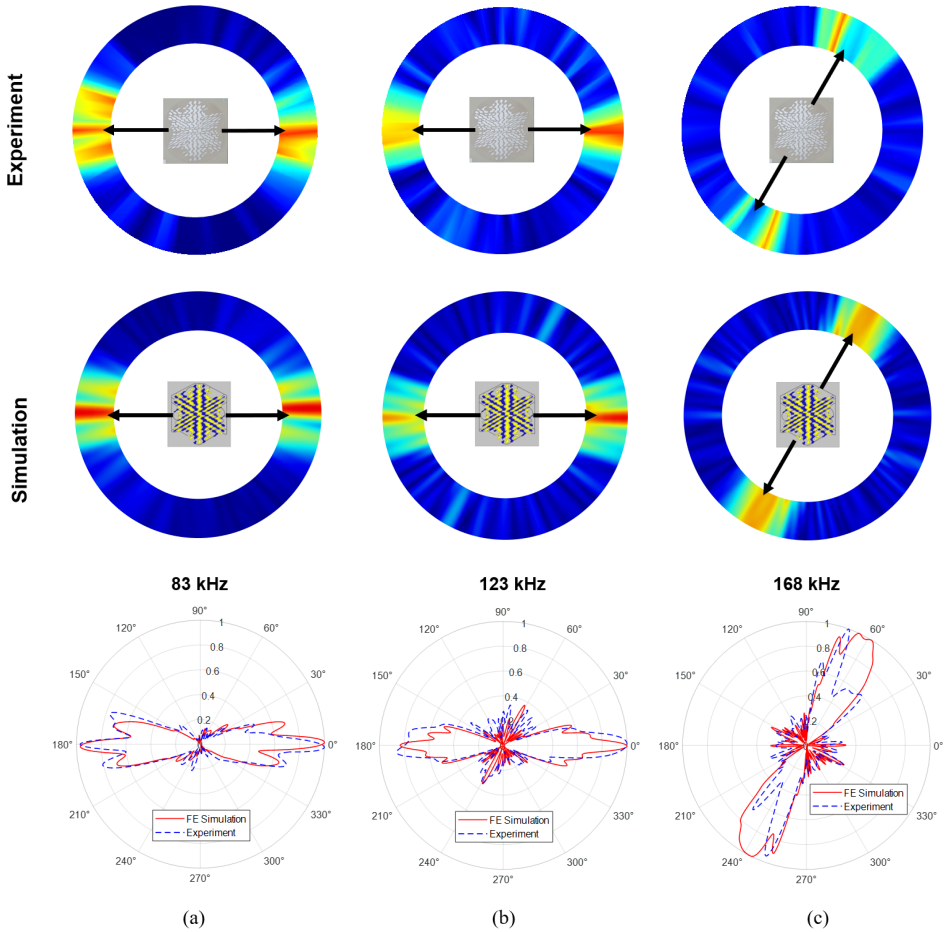

Fig. 8: Comparison of the experimental displacement wavefields and normalized beampatterns with those obtained from the FE simulation at different frequencies of a) 83 kHz (in 0°), b) 122 kHz (in 0°), and c) 168 kHz (in 60°) ; the black arrows indicate the desired wave directions

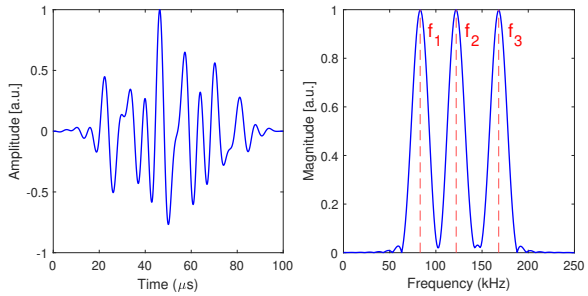

Fig. 9: Excitation signal with the carrier frequencies of $f_1 = 83$ kHz, $f_2 = 123$ kHz, and $f_3 = 168$ kHz and corresponding frequency spectrum, used for both experiments and simulations

the considered frequencies, which should be around 304 µs (83 kHz), 260 µs (123 kHz) and 232 µs (168 kHz). Furthermore, it is worth highlighting that this outcome is in very good agreement with the FE simulations reported in the second block row and also demonstrated via the simulated wavefield generated by transducer Tx shown in the snapshots of Fig. 11. A further corroboration of the above evidence stems from the response spectra depicted in the third block row, where the response spectra are plotted for both the experimental (blue) and simulated (FE) Rx data: two peak spectral values (indicated by vertical dashed red lines), located at $f_1 = 83$ kHz and $f_2 = 123$ kHz, respectively, can be identified for the FSAT transducer deployed in the horizontal direction, whilst one single peak at a frequency $f_3 = 168$ kHz can be recovered in the opposite direction, hence proving the MIMO communication capability of the realized FSAT device. It is worth mentioning that in both cases, a time window was selected for spectrum computation to exclude the initial portion of the Rx signals, known as acoustic cross-talk.

B. Parametric Analysis

This section presents a comprehensive systematic analysis aimed at investigating the robustness and performance of FSATs for the proposed GWs communication application. The study focuses on examining the influence of various parameters, including signal bandwidth, transducer dimensions, and carrier frequencies, on the device performance.

To conduct the analysis, four distinct FSATs were designed, each with varying side lengths of approximately 20mm, 40mm, 60mm, and 80mm, as illustrated in Fig. 12 . Among

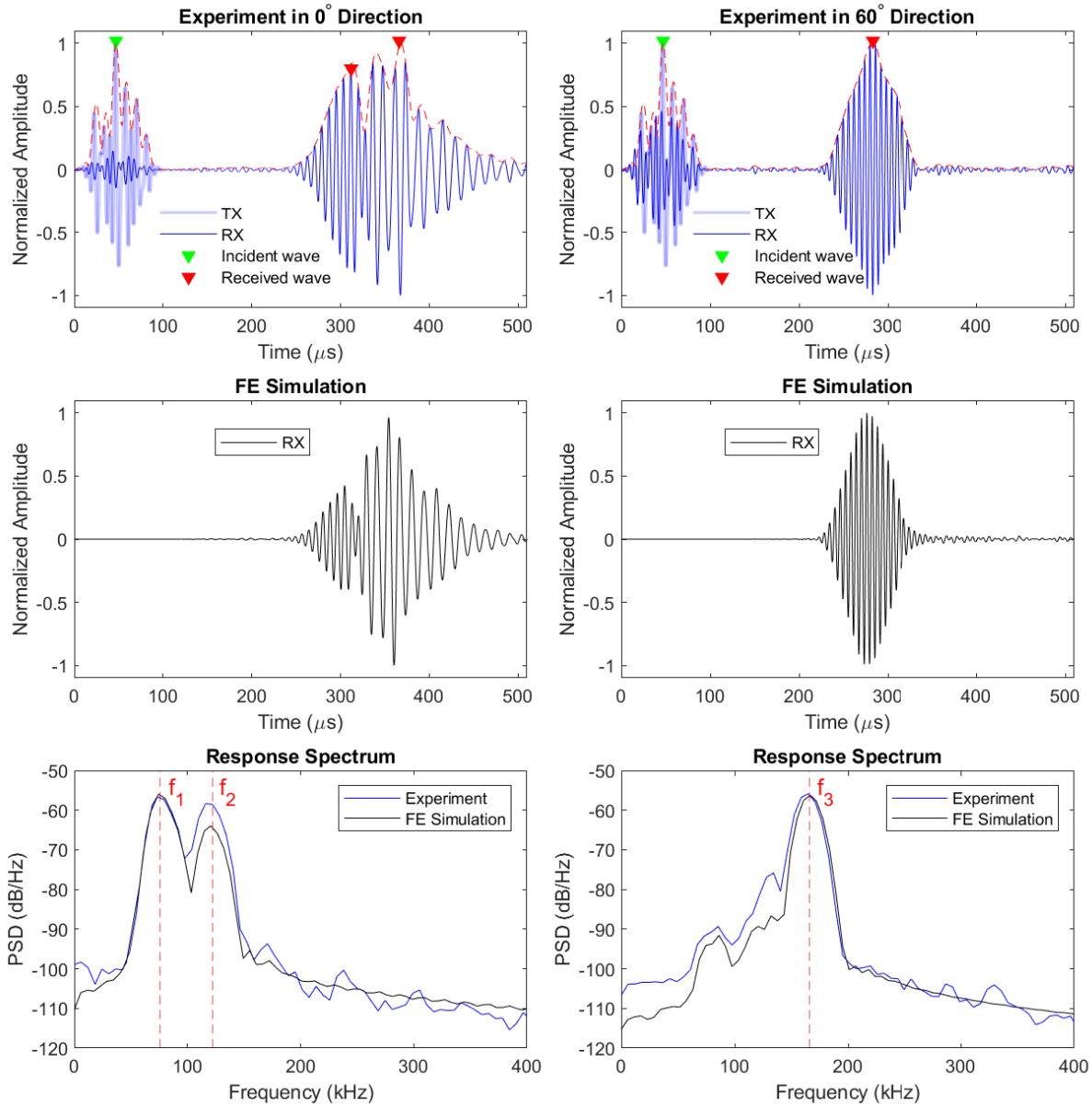

Fig. 10: Comparison of the experimental results with the FE simulation ones in the two target directions, 0° (left side) and 60°(right side). The actuation signal (TX) and the received signals (RX) have been shown together with their envelope, where the maxima of each wave packet are displayed for the sake of time of flight (TOF) estimations. In the response spectrum, the vertical dashed red lines refer to the frequencies of $f_1 = 83$ kHz, $f_2 = 123$ kHz , and $f_3 = 168$ kHz.

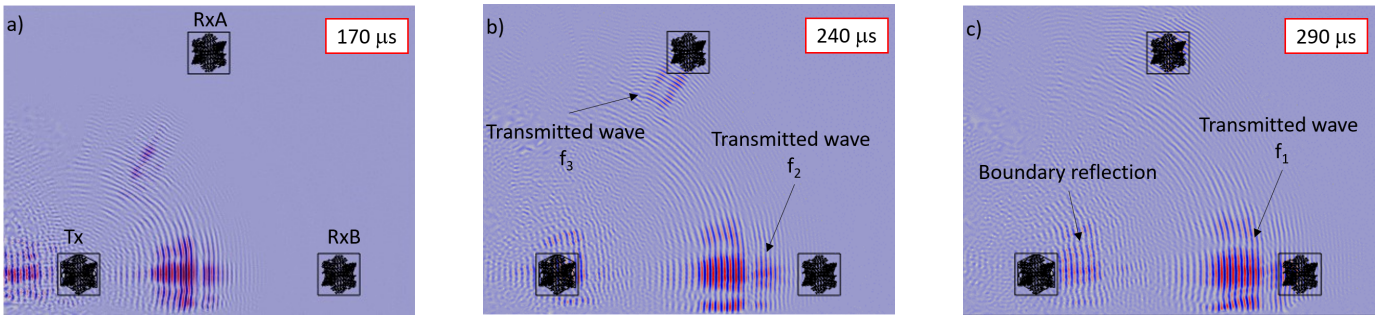

Fig. 11: Wavefield snapshots at successive time instants generated by the transducer (Tx) in the FE simulation, where the other two FSATs, namely RxA and RxB are the receivers in 60° and 0°, respectively.

these, the 60mm transducer was taken as the reference for comparison, as used in the previous sections. Based on the excellent consistency observed between the simulation and experimental results presented earlier, a series of simulations were performed for each transducer design, with symbol rates set at $5\,\mathrm{ksym/s}$, $10\,\mathrm{ksym/s}$, $15\,\mathrm{ksym/s}$, $20\,\mathrm{ksym/s}$, and $25\,\mathrm{ksym/s}$ (i.e., symbol period of $200\,\mu\mathrm{s}$, $100\,\mu\mathrm{s}$, $67\,\mu\mathrm{s}$, $50\,\mu\mathrm{s}$, and $40\,\mu\mathrm{s}$) . The simulations encompassed nine distinct frequencies for wave generation for each case, distributed among three main directions: 0°, 60°, and 120°, corresponding to frequencies of 50-83-123 kHz , 168-218-272 kHz , and 329-389-450 kHz , respectively. In total, the parametric analysis included 180 scenarios, covering all combinations of the four transducer sizes, five symbol rates, and nine frequencies.

During each simulation run, the transducer was excited with a specific Hann-windowed sinusoidal tone characterized by a symbol rate and frequency. The resulting displacement wavefield was recorded over a circle with a 300mm radius, centered at the transducer position, and encompassing sensing points at 5° interval. The captured signals were then used for further signal processing, including beampattern calculations and spectrum analysis. These procedures aimed to derive a metric that effectively showcases the steering performance of the proposed transducer in different scenarios. To this end, a metric was established, resembling the Signal-to-Noise Ratio (SNR) definition [31] . In this context, the metric was defined as the ratio between the amplitude of the spectrum at the central frequency of the selected channel, $P_{(\theta_L)}$, and the average of the amplitudes of the spectrum at the central frequencies corresponding to the other channels, $P_{(\theta_E)}$:

$$SNR_{(dB)} = 20\log\frac{P_{(\theta_L)}}{\Sigma P_{(\theta_E)}/(N-1)} \tag{10}$$

where N is the total number of channels. It is important to notice that this metric is computed to quantify the strength of the useful signal component with respect to the average spectral leakage on the remaining channels.

The analysis yielded significant observations regarding the transducer steering capabilities based on the defined SNR metric depicted in Fig. 13 , specifically presented for selected symbol rates to enhance clarity and visibility. First, regardless of transducer size or frequency, an increase in symbol rate (or decrease in signal duration) led to a decrease in SNR. However, the magnitude of SNR decrease was not uniform across all frequencies for different transducer sizes. Larger transducers consistently exhibited higher SNR values compared to smaller ones, indicating that larger transducers enhance the overall system performance and provide more robust steering capabilities. Moreover, higher frequencies demonstrated less sensitivity to transducer size variations, while lower frequencies showed a more substantial decrease in SNR with smaller transducers. This characteristic can be attributed to higher frequencies being associated with smaller wavelengths, resulting in reduced sensitivity to transducer dimensions. Interestingly, the analysis revealed that SNR variations caused by changing the symbol rate for different frequencies tended to converge in larger transducers. As transducer size increased, the SNR trends for different frequencies became more consistent, suggesting stable SNR behavior for larger transducers. Overall, the obtained results can aid in optimizing FSAT design parameters and provide an objective evaluation of the proposed system's performance, thereby advancing the understanding of FSATs' potential in practical communication implementations.

VI. Conclusion

In this work, a novel Piezoceramic prototype of FSATs has been presented to propose a novel generation of ultrasonic transducers which offer inherent beam steering capabilities and selective mode excitation feature. These unique features can allow the development of robust GW-based communication systems, which are still suffering from dispersive and multi-modal propagation, as well as multi-path fading, in state-of-the-art implementations. The FSAT has been thoroughly discussed, from its design principles based on the frequency directivity concept to the fabrication, fulfilling an exhaustive experimental characterization in terms of FE simulation, wavefield analysis, and laboratory experiments. The resulting transducer offers several essential features, such as inherent hardware directivity, spatial filtering, absence of multi-path interference and MIMO capabilities, which are essential in the realization of the next generation of ultrasonic GW-based acoustic communication systems. In these terms, FSATs can improve current implementations by proposing a minimally invasive and very compact solution capable to realize a spatial multiplexing strategy, similar to the one currently investigated in 5G communications, such that one single device can be exploited in place of a very dense array of piezoelectric sensors addressing the same task. The latter have been demonstrated in dedicated experiments in which the OOK modulation scheme has been adopted to successfully transmit and selectively receive different frequency tones along different directions.

The parametric analysis conducted for different scenarios offers valuable insights into the robustness and steering capabilities of FSAT for guided wave communication. By systematically examining transducer dimensions, symbol rate, and excitation frequencies, the study highlights the potential of larger transducers in enhancing SNR and overall system performance. Furthermore, understanding the frequency dependency on transducer size facilitates informed decisions for selecting FSAT configurations for various communication scenarios.

The current device faces a 180° ambiguity, leading to the simultaneous generation of waves in opposing directions. However, the authors are actively engaged in ongoing research to address these limitations and develope a more efficient device for communication applications. The goal is to enable unidirectional generation of guided waves, facilitating directional transmission, reducing wave back-reflection, and increasing the transmitted wave energy.

Acknowledgment

The research was conducted as part of the Guided Waves for Structural Health Monitoring (GW4SHM) project, which is financially supported by the Marie Skłodowska-Curie Actions

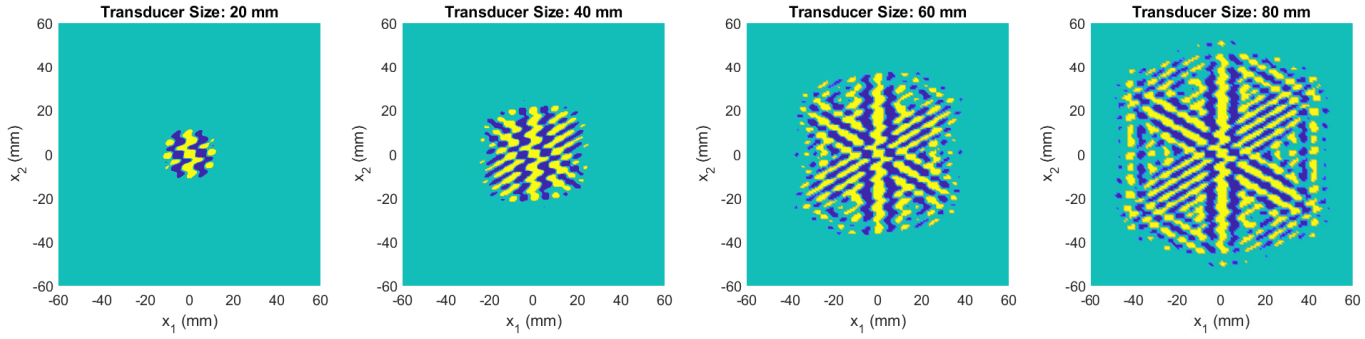

Fig. 12: The designed transducers with different sizes for systematic analysis

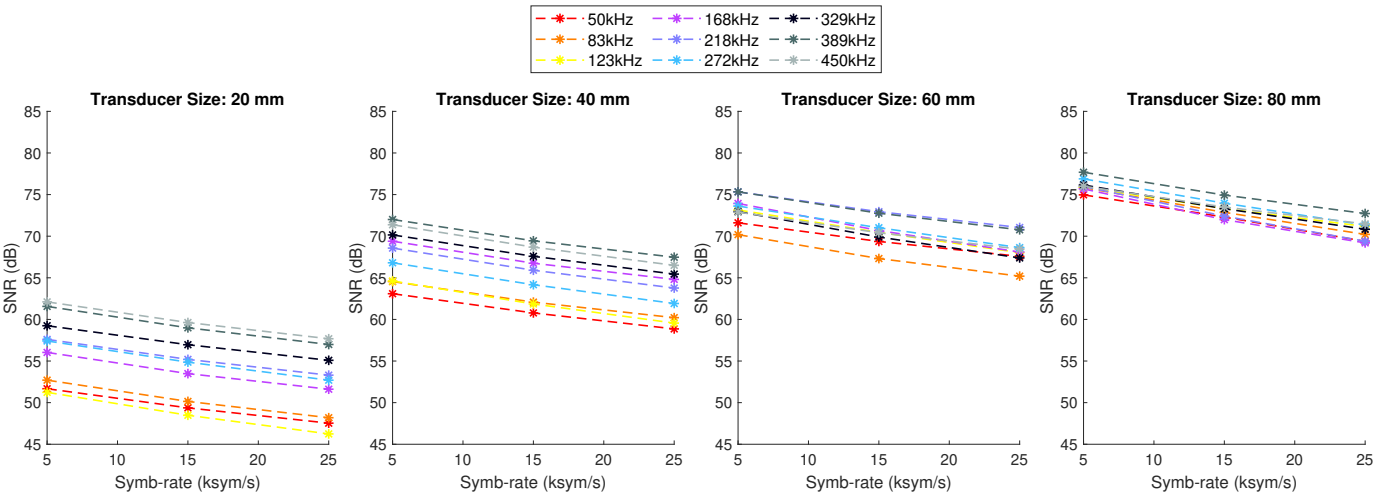

Fig. 13: SNR evaluation for different transducer sizes at varying symbol rates and carrier frequencies

Innovative Training Network, H2020 (Grant No. 860104) to which MM and LDM are grateful. LDM gratefully acknowledges funding from the ECSEL Joint Undertaking (JU) under grant agreement No 101007247, which receives support from the European Union's Horizon 2020 research and innovation programme and Finland, Germany, Ireland, Sweden, Italy, Austria, Iceland, Switzerland. JM gratefully acknowledges financial support by the German Research Foundation (DFG) under grant 349435502.

REFERENCES

[1] T. Clarke, P. Cawley, P. D. Wilcox, and A. J. Croxford, "Evaluation of the damage detection capability of a sparse-array guided-wave shm system applied to a complex structure under varying thermal conditions," *IEEE transactions on ultrasonics, ferroelectrics, and frequency control*, vol. 56, no. 12, pp. 2666–2678, 2009.

[2] H. Fu, Z. S. Khodaei, and M. F. Aliabadi, "An event-triggered energy-efficient wireless structural health monitoring system for impact detection in composite airframes," *IEEE Internet of Things Journal*, vol. 6, no. 1, pp. 1183–1192, 2018.

[3] H. Ge, D. Chua Kim Huat, C. G. Koh, G. Dai, and Y. Yu, "Guided wave–based rail flaw detection technologies: state-of-the-art review," *Structural Health Monitoring*, vol. 21, no. 3, pp. 1287–1308, 2022.

[4] P. Khalili and F. Cegla, "Excitation of single-mode shear-horizontal guided waves and evaluation of their sensitivity to very shallow crack-like defects," *IEEE Transactions on Ultrasonics, Ferroelectrics, and Frequency Control*, vol. 68, no. 3, pp. 818–828, 2020.

[5] W. Wu, M. Malik, S. Cantero-Chinchilla, T. Lawrie, W. Yan, G. Tanner, R. Remenyte-Prescott, and D. Chronopoulos, "Guided waves-based damage identification in plates through an inverse bayesian process," *Ultrasonics*, p. 106773, 2022.

[6] L. Yu and V. Giurgiutiu, "In situ 2-d piezoelectric wafer active sensors arrays for guided wave damage detection," *Ultrasonics*, vol. 48, no. 2, pp. 117–134, 2008.

[7] C. Xu, L. Peng, and M. Deng, "Phased array imaging for damage localization using multi-narrowband lamb waves," *Mechanical Systems and Signal Processing*, vol. 190, p. 110134, 2023.

[8] M. Mitra and S. Gopalakrishnan, "Guided wave based structural health monitoring: A review," *Smart Materials and Structures*, vol. 25, no. 5, p. 053001, 2016.

[9] C. Kexel, T. Maetz, M. Mälzer, and J. Moll, "Ultrasonic data transmission across metal structures affected by environmental conditions," *Journal of Sound and Vibration*, vol. 490, p. 115691, 2021.

[10] Z. Liu, Q. Xu, Y. Gong, C. He, and B. Wu, "A new multichannel time reversal focusing method for circumferential lamb waves and its applications for defect detection in thick-walled pipe with large-diameter," *Ultrasonics*, vol. 54, no. 7, pp. 1967–1976, 2014.

[11] C. Xu, H. Zuo, and M. Deng, "Dispersive music algorithm for lamb wave phased array," *Smart Materials and Structures*, vol. 31, no. 2, p. 025033, 2022.

[12] R. Sicard, J. Goyette, and D. Zellouf, "A saft algorithm for lamb wave imaging of isotropic plate-like structures," *Ultrasonics*, vol. 39, no. 7, pp. 487–494, 2002.

[13] M. Mohammadgholiha, F. Zonzini, and L. De Marchi, "Enabling spatial multiplexing in guided waves-based communication: the case of quadrature amplitude modulation realized via discrete frequency steerable acoustic transducers," in *2022 IEEE International Ultrasonics Symposium (IUS)*. IEEE, 2022.

[14] C. P. Dienel, H. Meyer, M. Werwer, and C. Willberg, "Estimation of airframe weight reduction by integration of piezoelectric and guided wave–based structural health monitoring," *Structural Health Monitoring*, vol. 18, no. 5-6, pp. 1778–1788, 2019.

[15] A. Heifetz, D. Shribak, X. Huang, B. Wang, J. Saniie, J. Young, S. Bakhtiari, and R. B. Vilim, "Transmission of images with ultrasonic elastic shear waves on a metallic pipe using amplitude shift keying pro-

tocol," *IEEE Transactions on Ultrasonics, Ferroelectrics, and Frequency Control*, vol. 67, no. 6, pp. 1192–1200, 2020.

[16] S. Chakraborty, G. J. Saulnier, K. W. Wilt, E. Curt, H. A. Scarton, and R. B. Litman, "Low-power, low-rate ultrasonic communications system transmitting axially along a cylindrical pipe using transverse waves," *IEEE transactions on ultrasonics, ferroelectrics, and frequency control*, vol. 62, no. 10, pp. 1788–1796, 2015.

[17] F. Zonzini, L. De Marchi, N. Testoni, and A. Marzani, "Direct spread spectrum modulation and dispersion compensation for guided wave-based communication systems," in *2019 IEEE International Ultrasonics Symposium (IUS)*. IEEE, 2019, pp. 2500–2503.

[18] M. Mälzer, C. Kexel, T. Maetz, and J. Moll, "Combined inspection and data communication network for lamb-wave structural health monitoring," *IEEE transactions on ultrasonics, ferroelectrics, and frequency control*, vol. 66, no. 10, pp. 1625–1633, 2019.

[19] C. Kexel, T. Maetz, M. Maelzer, and J. Moll, "Digital communication across orthotropic composite components using guided waves," *Composite Structures*, vol. 209, pp. 481–489, 2019.

[20] Y. Jin, Y. Ying, and D. Zhao, "Data communications using guided elastic waves by time reversal pulse position modulation: Experimental study," *Sensors*, vol. 13, no. 7, pp. 8352–8376, 2013.

[21] P. Anuradha, R. Arabelli, K. Rajkumar, and C. Padmaja, "Mimo-ofdm based high-rate information transmission through ultrasonic," in *AIP Conference Proceedings*, vol. 2418, no. 1. AIP Publishing LLC, 2022, p. 030059.

[22] O. A. Márquez Reyes, J. Moll, F. Zonzini, M. Mohammadgholiha, and L. De Marchi, "Quadrature amplitude modulation for acoustic data communication in ultrasonic structural health monitoring systems," in *Quantitative Nondestructive Evaluation*, vol. 85529. American Society of Mechanical Engineers, 2021, p. V001T16A001.

[23] M. Mohammadgholiha, A. Palermo, N. Testoni, J. Moll, and L. De Marchi, "Finite element modeling and experimental characterization of piezoceramic frequency steerable acoustic transducers," *IEEE Sensors Journal*, vol. 22, no. 14, pp. 13 958–13 970, 2022.

[24] E. Baravelli, M. Senesi, M. Ruzzene, L. De Marchi, and N. Speciale, "Double-channel, frequency-steered acoustic transducer with 2-d imaging capabilities," *IEEE transactions on ultrasonics, ferroelectrics, and frequency control*, vol. 58, no. 7, pp. 1430–1441, 2011.

[25] M. Eybpoosh, M. Berges, and H. Y. Noh, "Sparse representation of ultrasonic guided-waves for robust damage detection in pipelines under varying environmental and operational conditions," *Structural Control and Health Monitoring*, vol. 23, no. 2, pp. 369–391, 2016.

[26] S. Yu, C. Fan, and Y. Zhao, "A rapid 2d-fdtd method for damage detection in stiffened plate using time-reversed lamb wave," *Structural Health Monitoring*, p. 14759217231158049, 2023.

[27] M. Senesi and M. Ruzzene, "A frequency selective acoustic transducer for directional lamb wave sensing," *The Journal of the Acoustical Society of America*, vol. 130, no. 4, pp. 1899–1907, 2011.

[28] M. Dibiase, M. Mohammadgholiha, and L. De Marchi, "Optimal array design and directive sensors for guided waves doa estimation," *Sensors*, vol. 22, no. 3, p. 780, 2022.

[29] "COMSOL Multiphysics v. 5.6. www.comsol.com. COMSOL AB, Stockholm, Sweden."

[30] B. Ghose and K. Balasubramaniam, "Finite element modeling and simulation of ultrasonic guided wave propagation using frequency response analysis," in *Proceedings of the 14th Asia-Pacific Conference on NDT*, 2013.

[31] S. K. Pedram, S. Fateri, L. Gan, A. Haig, and K. Thornicroft, "Split-spectrum processing technique for snr enhancement of ultrasonic guided wave," *Ultrasonics*, vol. 83, pp. 48–59, 2018.